European Cells and Materials Vol.55 2026 (pages 63–79) DOI: 10.22203/eCM.v055a05 ISSN 1473-2262

Original Article

MICRONEEDLE-MEDIATED DELIVERY OF AN NIR-TRIGGERED NANOAGENT FOR SYNERGISTIC ANTI-BIOFILM INFECTION THERAPY

F.F. Chen[1,§], L.S. Zhang[2,§], L.Y. Wang[3], H.Y. Zhu[1], K. Ma[1], N.N. Yang[1], X.L. Meng[1], Z.Y. Pang[1,*] and D.D. Xu[4,*]

[1]Department of Emergency Medicine, The First Affiliated Hospital of Zhengzhou University, 450052 Zhengzhou, Henan, China
[2]School of Pharmaceutical Science, Zhengzhou University, 450001 Zhengzhou, Henan, China
[3]College of Arts & Sciences, Boston University, Boston, MA 02215, USA
[4]Department of Orthopedics, The First Affiliated Hospital of Zhengzhou University, 450052 Zhengzhou, Henan, China
[§]These authors contributed equally.

Abstract

Background: Post-surgical biofilm infections present a major clinical challenge due to their exceptional tolerance to antibiotics and the physical barrier of extracellular polymeric substance (EPS), calling for innovative non-antibiotic therapeutic strategies. **Methods**: We engineered a synergistic platform by constructing curcumin-loaded iron-based metal-organic framework (MIL@Cur) nanoparticles and incorporating them into a dissolvable hyaluronic acid-based hydrogel to fabricate composite microneedles (MIL@Cur microneedle (FCMN)). The system was characterized for its physicochemical properties and evaluated for antibacterial efficacy *in vitro* and in a murine methicillin-resistant *staphylococcus aureus* (MRSA)-infected wound model. **Results**: The MIL@Cur nanoparticles demonstrated well-defined morphology, high photothermal conversion efficiency (reaching >50 °C under laser irradiation), and pH-responsive drug release. *In vitro*, MIL@Cur with laser irradiation achieved synergistic bacterial eradication through photothermal therapy and iron-overload-induced chemodynamic therapy (CDT), while also disrupting pre-formed biofilms and inhibiting new biofilm formation via quorum sensing (QS) suppression. The FCMN patch exhibited excellent mechanical strength and efficient transdermal delivery. *In vivo*, the FCMN + Laser group showed accelerated wound closure, ∼ 2-log reduction in bacterial load, enhanced collagen deposition and angiogenesis, and no systemic toxicity. **Conclusions**: This microneedle-mediated platform effectively combines multiple antimicrobial modalities, providing a powerful and translatable strategy for treating stubborn biofilm infections and promoting wound repair.

Keywords: Microneedle, metal-organic framework, photothermal therapy, iron overload, biofilm eradication.

***Address for correspondence**: D.D. Xu, Department of Orthopedics, The First Affiliated Hospital of Zhengzhou University, 450052 Zhengzhou, Henan, China. Email: zdyfyxdd@zzu.edu.cn; Z.Y. Pang, Department of Emergency Medicine, The First Affiliated Hospital of Zhengzhou University, 450052 Zhengzhou, Henan, China. Email: pzygogogo@126.com.

Introduction

Postoperative bacterial infections, particularly those caused by drug-resistant bacteria leading to biofilm formation, pose a severe challenge in modern healthcare [1–3]. Biofilms are structured microbial communities that form when bacteria adhere to surfaces and become encased in a self-produced extracellular polymeric substance (EPS) [4,5]. This three-dimensional matrix not only provides a physical barrier that significantly impedes the penetration of antibiotics and attacks by host immune cells but also creates a unique microenvironment that promotes high levels of bacterial drug resistance and persistence, often resulting in chronic, difficult-to-treat infections that increase complexity and cost of care [6,7]. Although the development of novel antibiotics continues, its pace lags far behind the rapid evolution of bacterial resistance [8]. Therefore, there is an urgent need to develop innovative anti-infection strategies that can circumvent traditional antibiotic mechanisms, specifically targeting the structural characteristics of biofilms [9,10].

The rise of nanomedicine in recent years offers promising solutions to this challenge [11–13]. Among these, metal-organic frameworks (MOFs) have garnered significant attention due to their tunable structures, high porosity, and good biocompatibility [14–16]. Iron-based MOFs hold unique multifunctional promise for such ap-

plications. First, they display excellent photothermal conversion in the near-infrared (NIR) region. As efficient photothermal agents, they produce localized high temperatures under laser irradiation, physically disrupting bacterial membranes [17]. Second, the iron ions in their framework serve as ideal Fenton-reaction catalysts [18]. In the acidic milieu of infection sites, these ions convert bacterially overexpressed hydrogen peroxide (H_2O_2) into highly toxic hydroxyl radicals, inducing oxidative stress and bacterial death through chemodynamic therapy (CDT) [19,20]. Moreover, released iron ions trigger an "iron overload" effect inside bacterial cells. This disrupts their iron metabolic homeostasis, accelerating their demise from within [21]. However, a single sterilization mode is often insufficient to eradicate structurally complex biofilms and fails to effectively prevent their regrowth. Unlike the direct bactericidal action of traditional antibiotics, curcumin acts as a potent bacterial quorum sensing (QS) inhibitor. By interfering with chemical signal communication between bacteria, it effectively suppresses their aggregation, virulence factor secretion, and biofilm formation, while also promoting the loosening and disintegration of established biofilms [22,23]. Combining curcumin with iron-based MOFs to construct nanohybrid materials not only preserves the direct bactericidal function of MOFs but also endows them with the ability to "inhibit formation" and "promote disintegration" of biofilms, achieving synergistic suppression against both planktonic bacteria and biofilm pathogens.

Although nanomedicines demonstrate excellent performance *in vitro*, their effective delivery *in vivo* is crucial for therapeutic success. Traditional administration methods such as intravenous injection or topical application often fail to ensure adequate drug penetration through the skin barrier and accumulation at deep infection sites [24,25]. Furthermore, the extracellular polymeric matrix formed by biofilms severely hinders drug permeation, frequently leading to treatment failure. Hydrogel microneedle (MN) technology provides an elegant solution to this delivery challenge [26–28]. Comprising arrays of hundreds of micron-sized needles, this technology can painlessly penetrate the stratum corneum, delivering drugs directly to the dermal infection layer like a "submarine". By encapsulating nanomedicines within hydrogel microneedles, this approach not only protects drug activity but also enables rapid drug release upon needle insertion and subsequent dissolution, creating a high-concentration drug reservoir at the infection site for precise, uniform, and highly efficient targeted therapy. Based on these strategies, this study successfully designed and constructed a synergistic therapeutic platform integrating iron-based MOFs, curcumin, and hydrogel microneedles. The platform utilizes microneedles for accurate transdermal drug delivery. Upon activation by NIR laser, the nanomedicine simultaneously executes photothermal therapy to directly kill bacteria, releases iron ions to induce iron overload/CDT, and releases curcumin to inhibit the QS system, thereby dismantling and suppressing biofilm formation. This multi-mechanism synergy of "membrane disruption-bacterial killing-biofilm inhibition" aims to achieve comprehensive and efficient eradication of stubborn bacterial biofilm infections, providing a solid theoretical and experimental foundation for developing novel anti-biofilm infection therapies.

Materials and Methods

Synthesis of MIL-101(Fe) Nanoparticles

MIL-101(Fe) nanoparticles were synthesized via a one-step solvothermal method [29]. Briefly, 300 mg of ferric chloride hexahydrate ($FeCl_3 \cdot 6H_2O$, #236489, Sigma-Aldrich, St. Louis, Missouri, USA) and 166 mg of terephthalic acid (T0025, TCI Chemicals, Tokyo, Japan) were dissolved in 15 mL of anhydrous N, N-Dimethylformamide (DMF, #227056, Sigma-Aldrich, USA) with magnetic stirring for 30 minutes. The mixture was then transferred into a 25 mL Teflon-lined stainless-steel autoclave and heated at 110 °C for 12 hours. After cooling to room temperature naturally, the resulting brown precipitate was collected by centrifugation at 10,000 rpm for 10 minutes. The product was washed thoroughly with DMF and absolute ethanol (#459844, Sigma-Aldrich, USA) three times each to remove unreacted precursors. Finally, the purified MIL-101(Fe) nanoparticles were dried under vacuum at 60 °C for 12 hours, yielding a brown powder that was stored in a desiccator for further use.

Preparation of Curcumin-Loaded Iron-Based Metal-Organic Framework (MIL@Cur) Nanoparticles

Curcumin (C1386, Sigma-Aldrich, USA) was loaded into the MIL-101(Fe) nanoparticles via a solution immersion method. Specifically, 20 mg of the as-synthesized MIL-101(Fe) nanoparticles were dispersed in 10 mL of ethanol. Subsequently, 20 mg of curcumin (corresponding to a 1:1 mass ratio, as optimized from the drug loading efficiency experiments) was dissolved in 5 mL of ethanol and added dropwise to the MIL-101(Fe) dispersion under magnetic stirring. The mixture was stirred continuously at room temperature for 24 hours in the dark to allow for sufficient diffusion and loading of curcumin into the MOF pores. After the reaction, the loaded nanoparticles (MIL@Cur) were collected by centrifugation at 10,000 rpm for 10 minutes and washed with ethanol three times to remove superficially adsorbed curcumin. The final product was vacuum-dried at 40 °C for 6 hours.

Material Characterization

The morphology and size of the nanoparticles were examined using a transmission electron microscope (TEM, JEM-1400Flash, JEOL Ltd., Tokyo, Japan) operating at an acceleration voltage of 120 kV. Elemental composition and distribution were analyzed via energy-dispersive X-ray spectroscopy (EDS) using the X-MaxN 80T Silicon

Drift Detector (SDD) detector (Oxford Instruments, Abingdon, Oxfordshire, UK) attached to the TEM. The hydrodynamic diameter and zeta potential of the nanoparticles were measured using a dynamic light scattering (DLS) analyzer (Zetasizer Nano ZS, Malvern Panalytical Ltd., Malvern, Worcestershire, UK) at 25 °C. A standard curve for curcumin was established by measuring the absorbance (425 nm) of a series of curcumin/ethanol solutions with known concentrations (0, 5, 10, 20, 40, 60 μg/mL) using a UV-Vis spectrophotometer (UV-2600, Shimadzu Corporation, Kyoto, Japan). The drug loading efficiency (DLE) was calculated using the following formulas:

DLE (%) = (Weight of loaded curcumin / Weight of initial curcumin fed) × 100 %

The weight of loaded curcumin was determined by subtracting the amount of curcumin in the combined supernatants (from loading and washing steps) from the initial amount fed, using the standard curve for quantification.

In Vitro Performance Evaluation

In vitro release profile: 5 mg of MIL@Cur nanoparticles were dispersed in 10 mL of phosphate-buffered saline (PBS, 10010023, Thermo Fisher Scientific, Waltham, Massachusetts, USA) at different pH values (5.0, 6.0, 7.0), placed in a dialysis bag with a molecular weight cutoff of 8–14 kDa, and immersed in 50 mL of the corresponding PBS release medium. The system was incubated in a thermostatic shaker at 37 °C and 100 rpm in the dark. At predetermined time intervals (0, 2, 4, 8, 12, 24, 36, 48 hours), 1 mL of the external release medium was sampled and replaced with an equal volume of fresh, pre-warmed buffer. The collected samples were centrifuged, and the supernatants were used to determine curcumin concentration (425 nm) and iron ion concentration (using an iron assay kit, ab83366, Abcam, Cambridge, UK).

Photothermal performance measurement: 1 mL of PBS solution containing MIL@Cur nanoparticles (200 μg/mL) was placed in a quartz cuvette and irradiated with an 808 nm NIR laser at different power densities vertically for 5 minutes. The temperature change of the solution at different laser powers was monitored and recorded in real-time using an infrared thermal imaging camera. Photostability was assessed by subjecting the solution to five consecutive laser on (5 minutes)/off (cooling to room temperature) cycles.

Cytotoxicity Assay

The cytotoxicity of MIL@Cur nanoparticles was evaluated against murine-drived macrophage RAW264.7 cells (#CL-0190, Procell System®, Wuhan, China), which were authenticated by Short Tandem Repeat (STR) analysis and confirmed to be mycoplasma-free. Briefly, RAW264.7 cells were seeded in a 96-well plate at a density of 1×10^4 cells per well and cultured for 24 hours to allow for cell attachment. The culture medium was then replaced with fresh medium containing MIL@Cur nanoparticles at various final concentrations (10, 20, 50, 100, and 200 μg/mL). Wells containing cells with culture medium only served as the negative control (100 % viability). After 24 hours of co-incubation, the medium was carefully removed, and each well was washed with PBS. Subsequently, 100 μL of fresh medium containing 10 % (v/v) cell counting kit-8 (CCK-8, CK04, Dojindo, Kumamoto, Japan) solution was added to each well, followed by incubation at 37 °C for 2 hours. The absorbance of each well at 450 nm was measured using a microplate reader (BioTek Synergy H1, Winousky, Vermont, USA).

In Vitro Antibacterial and Anti-Biofilm Assays

Bacterial strains and experimental groups: Test strains included *staphylococcus aureus* (*S. aureus,* ATCC 25923, Manassas, Virginia, USA), methicillin-resistant *staphylococcus aureus* (MRSA, ATCC 43300), and *Escherichia coli* (*E. coli,* ATCC 35218). Experiments were divided into five groups. Control group: Treated with PBS; Curcumin group: Treated with free curcumin (40 μg/mL); MIL-101(Fe) group: Treated with MIL-101(Fe) nanoparticles (100 μg/mL); MIL@Cur group: Treated with MIL@Cur nanoparticles (100 μg/mL, equivalent to 40 μg/mL curcumin); MIL@Cur + Laser group: Treated with MIL@Cur nanoparticles (same concentration) followed by irradiation with an 808 nm NIR laser (Model: CME-L808, Zhongke microenerg Technology Co., Ltd., Beijing, China) for 5 minutes with power of 1.0 W/cm^2.

Anti-planktonic bacterial activity assessment: Bacteria in the mid-logarithmic growth phase were diluted to approximately 1×10^8 colony-forming units (CFU)/mL and co-incubated with an equal volume of the respective treatment solutions for 2 hours. For the MIL@Cur + Laser groups, laser irradiation was applied during incubation. After incubation, the bacterial suspensions were serially diluted, and 100 μL was spread onto LB agar plates (#244520, BD Diagnostics, Franklin Lake, New Jersey, USA). The plates were incubated at 37 °C for 24 hours, and the colony-forming units (CFU) were counted.

Bacterial Membrane Integrity Detection

Protein leakage assay: After co-incubation of bacteria with the treatments, the supernatant was collected by centrifugation. The protein concentration in the supernatant was measured using a Bicinchoninic acid (BCA) protein assay kit (#23225, Thermo Fisher Scientific, Waltham, Massachusetts, USA), with absorbance read at 562 nm.

O-Nitrophenyl β-D-galactopyranoside (ONPG) hydrolysis assay: Bacteria were resuspended in PBS containing 1 mM ONPG (N1127, Sigma-Aldrich, St. Louis, Missouri, USA). After adding the treatments and incubating, the absorbance at 405 nm was measured to monitor the hydrolysis product.

Table 1. Primer sequences.

Gene	Forward primer (5′ → 3′)	Reverse primer (5′ → 3′)
agrA	CCTGCACTGTAATGCCATCG	TGGTGCAGATAGTAGCGGTG
AtlE	GCTGGTGGTACAGCAAATCG	AGCACCAACACCGTTCAGAT
icaA	ATGGTCAAGCCCAGACAGAG	CGTGTTGTAACGCAATCCAG
icaD	AGCGAACGCAATAAATCACC	CGTATTTCCGCAGTAGTGCG
16S rRNA	GTAGGTGGCAAGCGTTATCC	CGCACATCAGCGTCAGTAAT

Intracellular Iron Content Measurement

After co-incubation of MRSA with the respective treatment groups (Control, Curcumin, MIL-101(Fe), MIL@Cur, MIL@Cur + Laser), the bacterial cells were collected by centrifugation and thoroughly washed with PBS to remove extracellular iron. The bacterial pellets were then lysed using a bacterial protein extraction reagent (#78243, Thermo Fisher Scientific, Waltham, Massachusetts, USA). The intracellular iron concentration in the lysates was quantified using an Iron Assay Kit according to the manufacturer's instructions, by measuring the absorbance at the recommended wavelength.

Intracellular Reactive Oxygen Species (ROS) Detection

The intracellular ROS levels in treated bacteria were measured using the fluorescent probe 2′,7′-Dichlorodihydrofluorescein diacetate (DCFH-DA, D399, Invitrogen, Carlsbad, California, USA). Briefly, MRSA suspensions were incubated with the different treatments. After treatment, bacterial cells were collected, washed with PBS, and then incubated with 10 μM DCFH-DA in the dark at 37 °C for 30 minutes. The fluorescence intensity of the oxidized product was measured using a fluorescence microplate reader (Excitation: 488 nm, Emission: 525 nm). The relative fluorescence intensity was calculated compared to the control group.

Iron Chelation Rescue Experiment

To confirm the specific role of iron-mediated toxicity in the antibacterial mechanism, a rescue experiment was performed using the iron chelator deferoxamine (DFO, D9533, Sigma-Aldrich, St. Louis, Missouri, USA). MRSA bacteria were pre-treated with 100 μM DFO for 30 minutes at 37 °C prior to being subjected to the standard MIL@Cur + Laser treatment. Following treatment, the bacterial suspensions were collected and stained using a commercial LIVE/DEAD BacLight ™ Bacterial Viability Kit (L7012, Invitrogen, USA) according to the manufacturer's protocol. Briefly, the bacteria were incubated with the SYTO 9 and Propidium Iodide (PI) dye mixture in the dark for 15 minutes. The stained bacteria were then immobilized on a glass slide and immediately visualized under a fluorescence microscope. SYTO 9 (green fluorescence) stains all bacteria, while PI (red fluorescence) only penetrates bacteria with compromised membranes, indicating dead cells.

Anti-Biofilm Activity Assessment

Biofilm inhibition: Bacteria and the respective treatments were added simultaneously to a 96-well plate and incubated statically at 37 °C for 24 hours to allow biofilm formation under treatment.

Biofilm disruption: Mature biofilms were first established by incubating bacteria in a 96-well plate for 24 hours. Then, the culture medium was removed, and the respective treatments were added to the pre-formed biofilms for another 24 hours.

After treatment, the biofilms were stained with 0.1 % (w/v) crystal violet solution (C0775, Sigma-Aldrich, USA). The bound dye was dissolved in 95 % ethanol, and the absorbance was measured at 595 nm. For viable bacterial counts within the biofilms, after treatment, the biofilms were gently washed with PBS, disaggregated via sonication, serially diluted, and plated for CFU counting.

Biofilm Structural Analysis by Confocal Laser Scanning Microscopy (CLSM)

Mature MRSA biofilms were prepared by incubating bacteria in glass-bottom culture plates for 24 hours. The pre-formed biofilms were washed, treated with MIL@Cur nanoparticles (100 μg/mL), and irradiated with an 808 nm NIR laser (1.0 W/cm^2, 5 minutes). After treatment, biofilms were washed and simultaneously stained with SYTO 9 (3 μM, 20 minutes; #S34854, Invitrogen, Carlsbad, California, USA) to label all bacterial cells and Concanavalin A-Alexa Fluor 647 conjugate (100 μg/mL, 30 minutes; #C21421, Invitrogen, Thermo Fisher Scientific, USA) to specifically label polysaccharides within the extracellular matrix. The biofilms were then gently washed to remove excess dye. The stained biofilms were imaged using a confocal laser scanning microscope (LSM 980 with Airyscan 2, Carl Zeiss AG, Oberkochen, Germany) with consistent settings. Z-stack images were acquired from multiple random fields. Using Imaris 10.1 software (Abingdon, Oxfordshire, UK), the biovolume of bacteria (SYTO 9 signal) and extracellular polysaccharides (ConA-647 signal), as well as the average biofilm thickness, were quantified.

Quorum Sensing (QS) Gene Expression Analysis

Gene expression analysis was performed on mature MRSA biofilms after 24 hours of treatment with the respective agents. Total RNA was extracted from the treated

biofilms using a commercial bacterial RNA extraction kit (#74104, Qiagen, Finlo, Hesse, Germany), including a step for DNase I (M0303S, New England Biolabs, Ipswich, Massachusetts, USA) treatment to remove genomic DNA contamination. The concentration and purity of the RNA were determined spectrophotometrically. First-strand Complementary DNA (cDNA) was synthesized from 1 μg of total RNA using a reverse transcription kit (RR047A, Takara Bio, Shiga, Japan) with random hexamers. Quantitative real-time polymerase chain reaction (qRT-PCR) was performed using SYBR Green Master Mix (#4309155, Applied Biosystems, South San Francisco, California, USA) on a real-time PCR system. The expression levels of key QS genes were analyzed using the comparative $2^{-\Delta\Delta Ct}$ method, with the bacterial *16S rRNA* gene serving as an internal reference control. The sequences of the specific primers used for each gene were provided in Table 1.

Fabrication and Characterization of the FCMN Patch

Microneedle fabrication: The MIL@Cur microneedles (FCMNs) were prepared using a centrifugal casting method [30]. First, 200 mg of poly(vinyl alcohol) (PVA, #363146, Sigma-Aldrich, St. Louis, Missouri, USA) and 50 mg of trehalose (T9531, Sigma-Aldrich, USA) were dissolved in 1 mL of deionized water to form a hydrogel prepolymer solution. Then, 50 mg of MIL@Cur nanoparticles were uniformly dispersed into this solution. The mixture was poured onto a polydimethylsiloxane (PDMS) microneedle mold and centrifuged at 4000 rpm for 10 minutes to ensure the needle cavities were fully filled. The mold was then frozen at –20 °C for 2 hours, followed by –80 °C for 2 hours, and finally lyophilized for 24 hours to obtain the dry, rigid FCMN patch.

Microneedle characterization: The morphology and elemental composition of the microneedles were examined using a field emission scanning electron microscope (FE-SEM, SU8010, Hitachi High-Technologies Corporation, Tokyo, Japan) equipped with an EDS. The mechanical strength of the FCMN was evaluated using a universal material testing system (Instron 5943, Norwood, Massachusetts, USA) equipped with a 50 N load cell. Skin insertion tests were performed on excised mouse skin. The patch was applied with gentle pressure and held for 5 minutes. After removal, the skin tissue was processed for histological sectioning and hematoxylin and eosin (H&E) staining. The sections were observed under a microscope to visualize and measure the depth of the microconduits created by the needles. To evaluate the local biocompatibility under repeated application conditions, FCMN patches were applied to the intact mouse skin for 10 minutes daily over three consecutive days. Macroscopic observations for signs of local irritation, including redness, swelling, or scabbing, were recorded daily.

Mouse Wound Infection Model

Sixty male BALB/c mice (6–8 weeks old; 20–22g) were purchased from Shanghai Model Organisms (Shanghai, China). The mice were housed under a standard 12-hour light/dark cycle. The temperature and humidity were maintained at 23 $\pm$ 2 °C and 50–60 %, respectively. A full-thickness skin wound with a diameter of 8 mm was created on the dorsum of each mouse. The wound was then inoculated with 20 μL of an MRSA suspension containing approximately 1×10^8 CFU to establish the infection model. Infected mice were randomly divided into five groups (n = 12 per group). Control group: No treatment; MN group: Application of a blank microneedle patch for 10 minutes; MIL@Cur group: Topical application of 100 μL of MIL@Cur nanoparticle suspension (5 mg/mL) onto the wound; FCMN group: Application of the MIL@Cur-loaded FCMN patch for 10 minutes; FCMN + Laser group: Application of the FCMN patch for 10 minutes, followed by irradiation of the wound with an 808 nm NIR laser (1.0 W/cm^2) for 5 minutes. The laser beam was adjusted to produce a circular spot with a diameter of $\sim$ 12 mm, which was larger than the wound diameter. This ensured the entire wound area received uniform irradiation. The distance between the laser aperture and the sample surface was fixed at 15 cm to achieve the desired spot size and power density. Investigators responsible for outcome assessment and data analysis were blinded to the group allocation throughout the experiment.

In Vivo Evaluation Metrics

Wound healing rate: Mice were anesthetized by intraperitoneal injection of sodium pentobarbital (40 mg/kg) and placed in a standardized position at each time point. Wounds were photographed alongside a ruler for scale using a high-resolution digital camera under consistent lighting conditions. The wound area was delineated and quantified in square millimeters using the standardized measurement tools in ImageJ2 software (Bethesda, Maryland, USA).

Bacterial burden: On designated days, mice were euthanized by intraperitoneal injection of an overdose of sodium pentobarbital (150 mg/kg). After the cessation of breathing was confirmed, the entire wound tissue, including a 2-mm margin of surrounding skin, was aseptically excised. The tissue was weighed, homogenized in 1 mL of sterile PBS using a mechanical homogenizer on ice, and serially diluted 10-fold in PBS. A 100-μL aliquot of each dilution was spread onto LB agar plates, which were then incubated at 37 °C for 24 hours. Bacterial colonies were counted, and the results were expressed as Log10 CFU per gram of tissue.

Histological analysis: On day 10, the entire wound tissue with surrounding edges was harvested and fixed in 4 % paraformaldehyde (#158127, Sigma-Aldrich, St. Louis, Missouri, USA) for 24 hours. Tissues were then processed

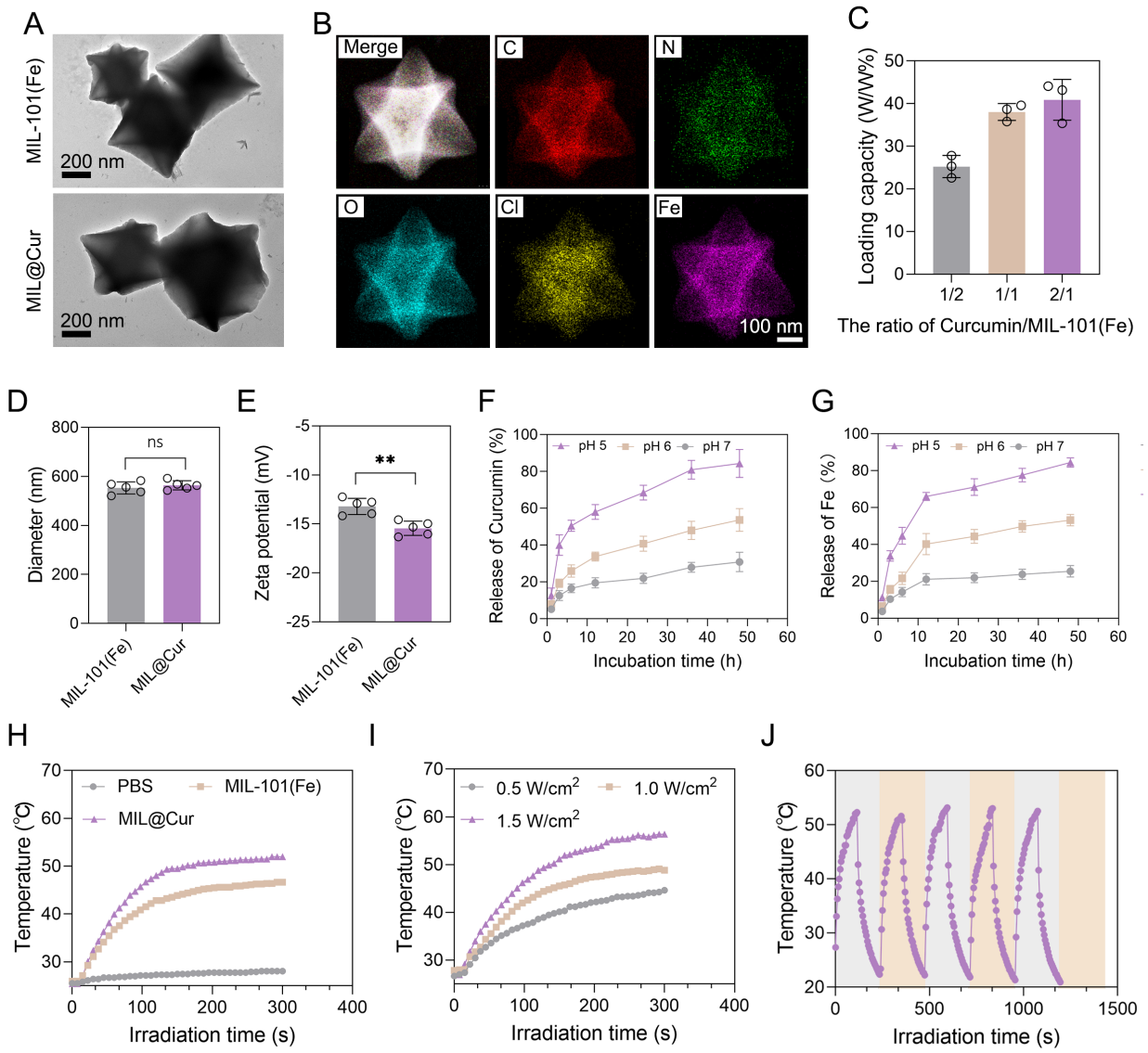

Fig. 1. Synthesis and characterization of MIL@Cur nanoparticles. (**A**) Representative TEM images of MIL-101(Fe) and MIL@Cur nanoparticles. Scale bars: 200 nm. (**B**) TEM-based elemental mapping of MIL@Cur showing the distribution of C, O, Fe, and N. Scale bar: 100 nm. (**C**) Drug loading efficiency of curcumin at different feeding mass ratios. n = 3. (**D**) Hydrodynamic diameter and (**E**) Zeta potential of MIL-101(Fe) and MIL@Cur nanoparticles. n = 5. (**F**) Cumulative release profile of curcumin and (**G**) iron ions from MIL@Cur in PBS at different pH values. n = 3. (**H**) Photothermal heating curves of PBS, MIL-101(Fe), and MIL@Cur under 808 nm laser irradiation. (**I**) Photothermal heating curves of MIL@Cur at different laser power densities. (**J**) Photothermal stability of MIL@Cur over five laser on/off cycles. MIL@Cur, curcumin-loaded iron-based metal-organic framework; PBS, phosphate-buffered saline; ns means no significant, $^{**}p < 0.01$. The images were plotted using GraphPad Prism 9.0 (San Diego, California, USA) and Adobe Photoshop 2023 software (San Jose, California, USA).

through a graded ethanol series, embedded in paraffin, and sectioned into 5-μm thick slices. For comprehensive analysis, sections were stained with: H&E staining following standard protocols to evaluate general tissue architecture and inflammatory cell infiltration; Masson's Trichrome staining to assess collagen deposition and fiber organization; immunohistochemical (IHC) staining for tumor necrosis factor-α (TNF-α), platelet endothelial cell adhesion molecule-1 (CD31), and transforming growth factor-β (TGF-β). Briefly, after antigen retrieval and blocking, sections were incubated overnight at 4 °C with primary antibodies against TNF-α (1:200, ab66579, Abcam, Cambridge, UK), CD31 (1:100, ab28364, Abcam, UK), and TGF-β (1:150, ab92486, Abcam, UK), followed by incubation with HRP-conjugated secondary antibodies (#7074S, Cell Signaling Technology, Danvers, Massachusetts, USA) and 3,3'-Diaminobenzidine (DAB) (SK-4100, Vector Laboratories, Newark, California, USA) development. Addi-

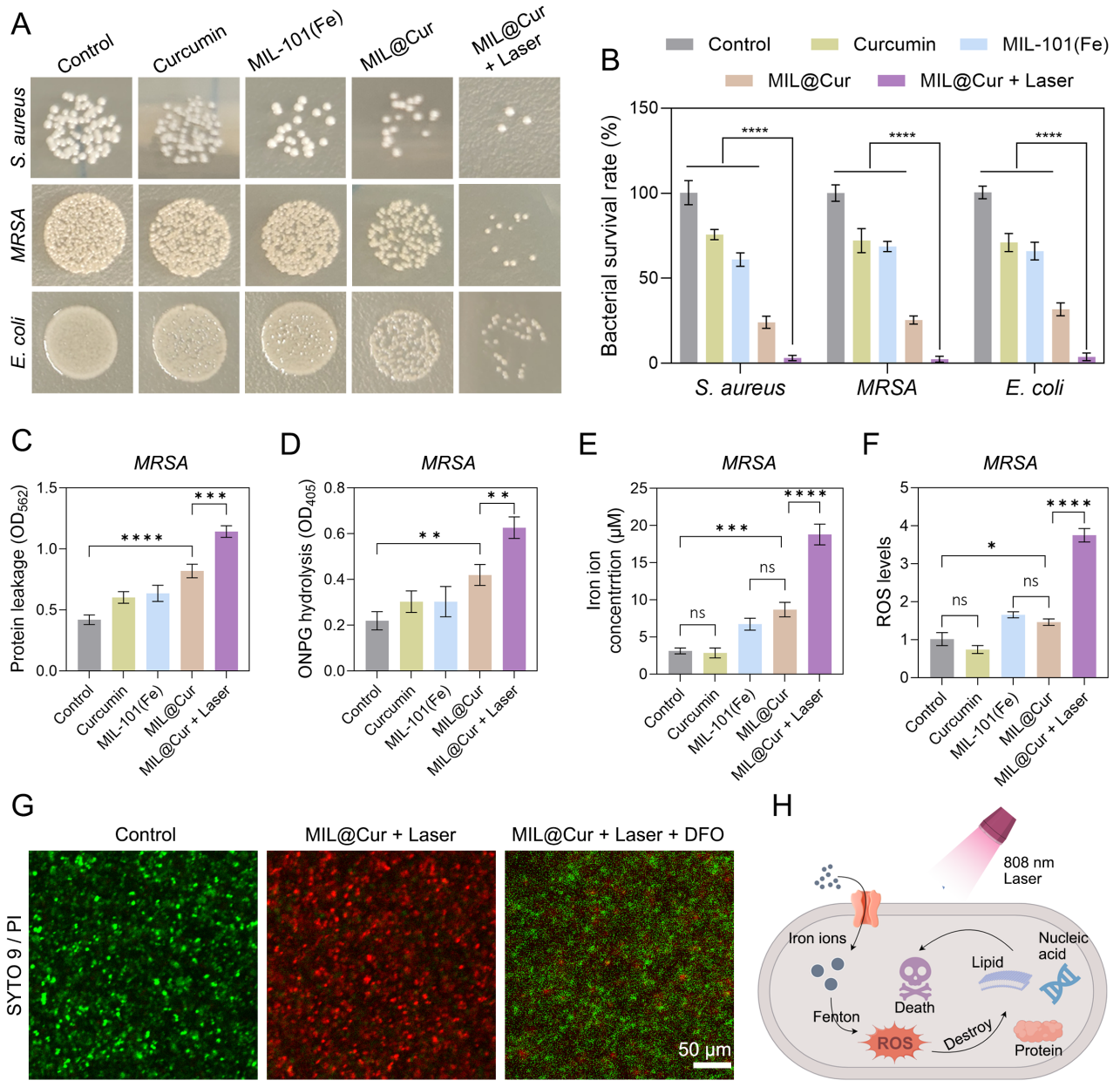

Fig. 2. ***In vitro*** **antibacterial activity against planktonic bacteria.** (**A**) Photographs and (**B**) corresponding quantitative survival rates of *S. aureus*, MRSA, and *E. coli* colonies after various treatments. n = 5. (**C**) Bacterial membrane integrity assessed by protein leakage assay. n = 3. (**D**) Bacterial membrane permeability evaluated by ONPG hydrolysis assay. n = 3. (**E**) Intracellular levels of iron ions in MRSA after different treatments. n = 3. (**F**) Intracellular ROS levels in MRSA after different treatments. n = 3. (**G**) Fluorescence microscopy images of live/dead stained MRSA (green: live bacteria; red: dead bacteria) and the rescue effect of the iron chelator DFO. Scale bars: 50 μm. (**H**) Schematic diagram of the bactericidal mechanism. MIL@Cur, curcumin-loaded iron-based metal-organic framework; *S. aureus*, *staphylococcus aureus*; MRSA, methicillin-resistant *staphylococcus aureus*; *E. coli*, *Escherichia coli*; ONPG, o-Nitrophenyl β-D-galactopyranoside; ROS, reactive oxygen species; DFO, deferoxamine. ns means no significant, *$p < 0.05$, **$p < 0.01$, ***$p < 0.001$, ****$p < 0.0001$. The images were plotted using GraphPad Prism 9.0 and Adobe Photoshop 2023 software.

tionally, the major organs (heart, liver, spleen, lungs, and kidneys) of mice in the control group and the FCMN + Laser group were collected and subjected to H&E staining for safety assessment. All stained sections were imaged under a light microscope. Semi-quantitative analysis was performed using ImageJ software, where five random fields per section were analyzed to determine the percentage of positively stained area for each marker.

Blood biochemical analysis: On day 10, blood was collected from the mouse orbital sinus into serum separation

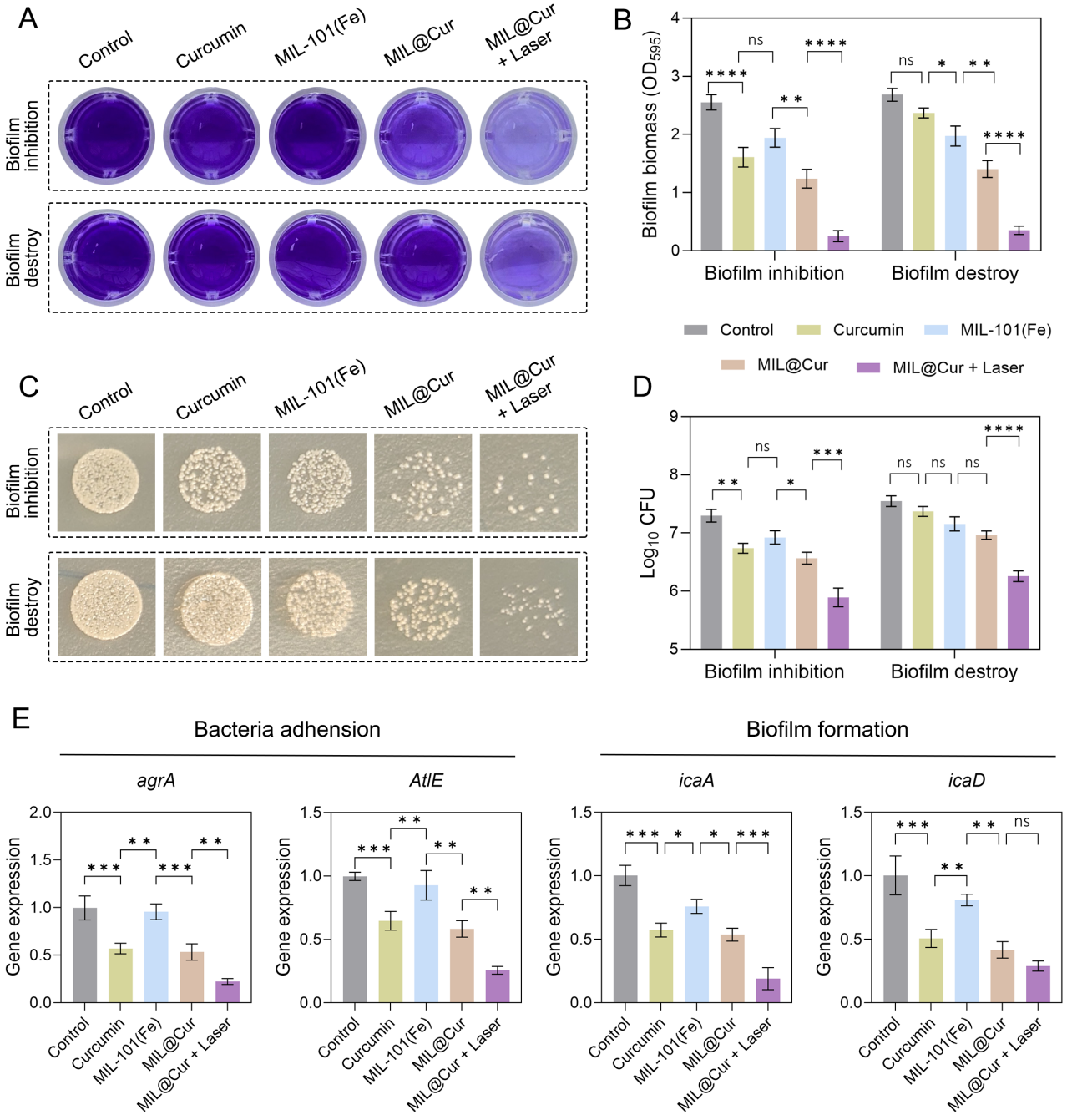

Fig. 3. *In vitro* anti-biofilm activity. (**A**) Crystal violet staining and (**B**) corresponding quantitative analysis of biofilms after various treatments. n = 3. (**C**) Photographs and (**D**) quantitative viable bacterial counts of bacteria recovered from disrupted biofilms after various treatments. n = 3. (**E**) Relative mRNA expression levels of key quorum sensing (*agrA*, *AtlE*) and biofilm-related (*icaA*, *icaD*) genes in MRSA biofilms after treatment. n = 5. MIL@Cur, curcumin-loaded iron-based metal-organic framework. ns means no significant, *$p < 0.05$, **$p < 0.01$, ***$p < 0.001$, ****$p < 0.0001$. The images were plotted using GraphPad Prism 9.0 and Adobe Photoshop 2023 software.

tubes. After clotting, samples were centrifuged at 3000 rpm for 15 minutes to obtain serum. The serum levels of alanine aminotransferase (ALT), aspartate aminotransferase (AST), blood urea nitrogen (BUN), and creatinine (CRE) were measured using commercial diagnostic kits (#Z002-1-1 and #Z003-1-1, Nanjing Jiancheng Bioengineering Institute, Nanjing, China) according to the manufacturer's instructions.

Statistical Analysis

All experimental data are presented as the mean ± standard deviation. Statistical comparisons between

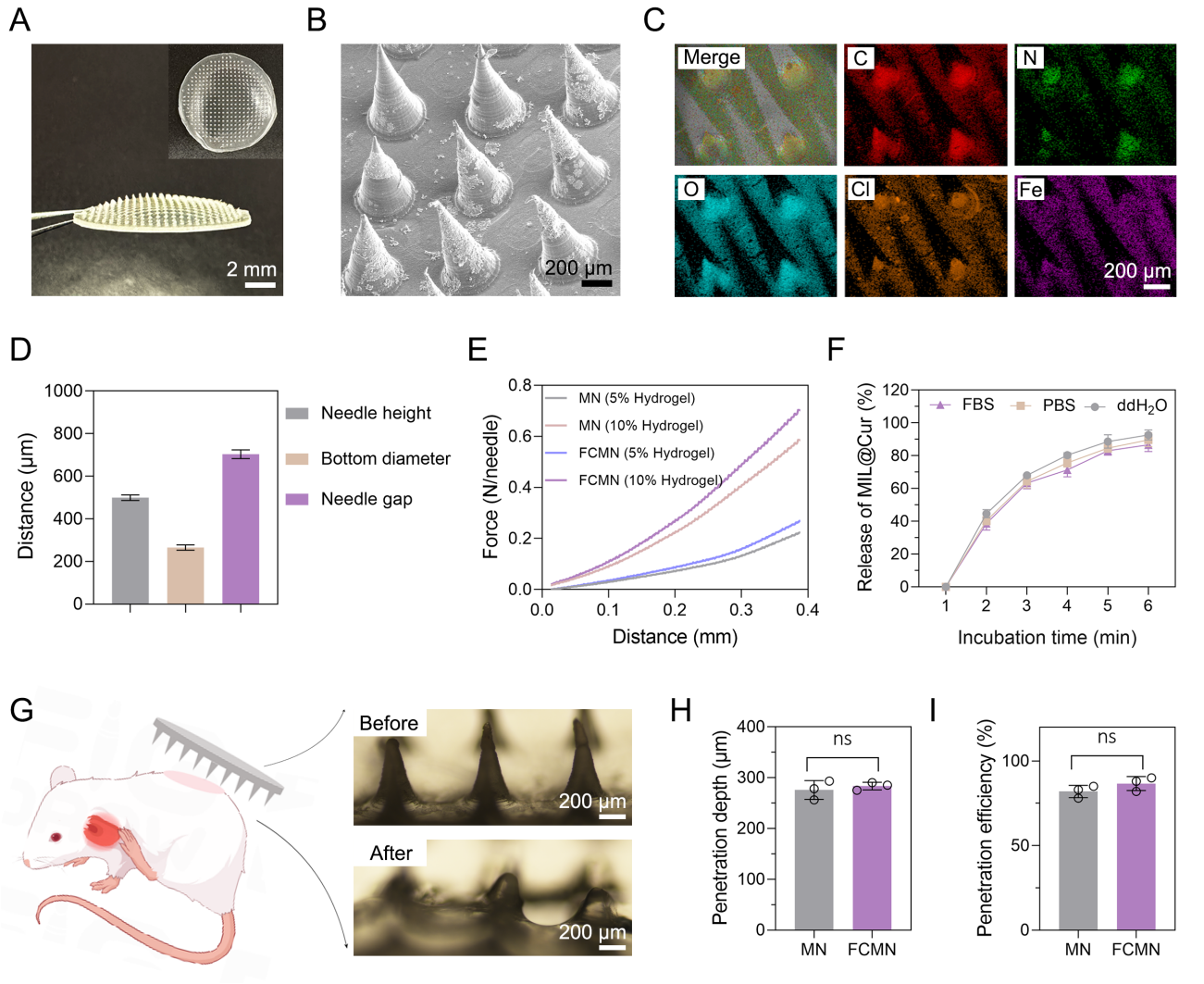

Fig. 4. Fabrication and characterization of the FCMN patch. (**A**) Macroscopic and (**B**) SEM images of the FCMN patch. Scale bars: 2 mm in **A**; 200 μm in **B**. (**C**) SEM-based elemental mapping of a single microneedle tip. Scale bar: 200 μm. (**D**) Schematic diagram illustrating the geometric dimensions of the microneedles. (**E**) Mechanical strength of a single microneedle assessed by compression testing. (**F**) *In vitro* drug release profile from FCMN in different media. n = 3. (**G**) Macroscopic images of mouse skin before and after FCMN application. Scale bars: 200 μm. (**H**) Statistical analysis of microneedle penetration depth. (**I**) Statistical analysis of microneedle penetration efficiency. MN, microneedle; FCMN, MIL@Cur microneedle; FBS, fetal bovine serum; PBS, phosphate-buffered saline; ns means no significant. The images were plotted using GraphPad Prism 9.0 and Adobe Photoshop 2023 software.

groups were performed using one-way analysis of variance (ANOVA) followed by Tukey's post-hoc test in GraphPad Prism 9.0 (San Diego, California, USA). A *p*-value of less than 0.05 ($p < 0.05$) was considered statistically significant.

Results

Synthesis and Characterization of MIL@Cur Nanoparticles

MIL-101(Fe) nanoparticles were successfully synthesized via a solvothermal method. TEM images revealed that both the pristine MIL-101(Fe) and the curcumin-loaded MIL@Cur nanoparticles maintained a well-defined hexagonal star-like morphology (Fig. 1**A**). Elemental mapping confirmed the homogeneous distribution of C, O, Fe, and the N signal from curcumin within the MIL@Cur structure (Fig. 1**B**). The drug loading efficiency was optimized, with a 1:1 mass ratio of curcumin to MIL-101(Fe) yielding an efficiency of approximately 38 %, which was selected for subsequent studies (Fig. 1**C**). DLS measurements showed that the hydrodynamic diameter of the nanoparticles changed from 553 ± 24.6 nm for MIL-101(Fe) to 563.6 ± 18.6 nm for MIL@Cur (Fig. 1**D**, $p > 0.05$), while the zeta potential became more negative, from –13.2 ± –0.8 mV to –15.5 ± –0.7 mV (Fig. 1**E**, $p < 0.05$). The MIL@Cur nanoparticles exhibited a pronounced pH-responsive release profile, with nearly 80 % of both curcumin and Fe ions released within 48 hours at pH 5.0, significantly faster than at neutral pH (Fig. 1**F,G**). Under 808 nm laser irradi-

ation (1.0 W/cm^2), the MIL@Cur solution demonstrated a rapid temperature increase to 52 °C within 2 minutes, superior to MIL-101(Fe) alone (Fig. 1**H**). Furthermore, both the heating rate and peak temperature increased with higher laser power (Fig. 1**I**). Notably, MIL@Cur maintained excellent photostability throughout multiple switching cycles (Fig. 1**J**). The RAW264.7 cells were incubated with a series of concentrations (10, 20, 50, 100, and 200 μg/mL) of MIL@Cur for 24 hours, and cell viability was assessed using a CCK-8 assay. As shown in **Supplementary Fig. 1**, even at the highest concentration of 200 μg/mL, the cell viability remained above 95 %, with no significant difference compared to the control group treated with fresh culture medium alone ($p > 0.05$).

In Vitro Antibacterial Activity Against Planktonic Bacteria

The antibacterial efficacy of MIL@Cur was evaluated against *S. aureus*, MRSA, and *E. coli*. Results showed that the MIL@Cur combined with laser treatment group exhibited the lowest number of colonies formed on agar plates (Fig. 2**A**), with bacterial survival rates of 3.1 ± 1.6 % (*S. aureus*), 2.4 ± 1.7 % (MRSA), and 3.8 ± 2.3 % (*E. coli*), significantly outperforming all other experimental groups (Fig. 2**B**, $p < 0.05$). Both the protein leakage assay (Fig. 2**C**) and the ONPG hydrolysis assay (Fig. 2**D**) indicated that the MIL@Cur + Laser treatment caused the most severe damage to bacterial membrane integrity ($p < 0.05$). Temperature monitoring confirmed that the bacterial suspension in the MIL@Cur + Laser group reached 50.3 °C upon irradiation (**Supplementary Fig. 2**). Additionally, MIL@Cur + Laser elevated intracellular iron concentrations in MRSA by 6-fold (Fig. 2**E**) and increased ROS levels by 3.7-fold (Fig. 2**F**), representing the most pronounced effect among all treatment groups. Live/dead staining visualized nearly complete bacterial killing (red fluorescence) in the MIL@Cur + Laser group, an effect that was markedly reversed by the iron chelator DFO (Fig. 2**G** and **Supplementary Fig. 3**). Based on the above results, we inferred the bactericidal mechanism of MIL@Cur + Laser (Fig. 2**H**). Excess iron ions induce ROS accumulation within bacteria, damaging nucleic acids and other active molecules, ultimately leading to iron-dependent bacterial death.

In Vitro Anti-Biofilm Activity

We further evaluated the therapeutic efficacy of MIL@Cur against bacterial biofilm infections. In terms of inhibiting new biofilm formation and disrupting established biofilms, the MIL@Cur + Laser-treated group exhibited the lightest crystal violet staining (Fig. 3**A**, $p < 0.05$) and the lowest corresponding absorbance (Fig. 3**B**, $p < 0.05$). Plate counting revealed that MIL@Cur + Laser reduced the viable bacterial load within the biofilm by approximately two orders of magnitude compared to the control group (Fig. 3**C, D**). In contrast, the free curcumin group, MIL-101(Fe) group, and MIL@Cur group exhibited less pronounced anti-biofilm activity. Furthermore, we performed CLSM to directly visualize and quantify the structural disintegration of the biofilm matrix. Three-dimensional reconstruction and quantitative analysis revealed that treatment with MIL@Cur + Laser significantly reduced both average biofilm thickness and EPS polysaccharide biovolume compared to all control groups (**Supplementary Fig. 4**). The molecular mechanism underlying this enhanced efficacy was investigated via qRT-PCR. The analysis indicated that MIL@Cur + Laser treatment most significantly downregulated key QS genes in MRSA ($p < 0.05$). This included *agrA* and *AtlE* genes associated with bacterial adhesion, as well as *icaA* and *icaD* genes linked to polysaccharide intercellular adhesin production and biofilm formation (Fig. 3**E**).

Fabrication and Characterization of the FCMN Patch

To enhance localized drug delivery efficiency, the MIL@Cur nanoparticles were incorporated into a hydrogel matrix to form a dissolvable MN patch, termed FCMN. The resulting FCMN patch displayed a uniform disc-like structure with a densely packed array of sharp, conical needles (Fig. 4**A, B**). Elemental mapping confirmed the successful and uniform distribution of the characteristic elements (C, O, Fe) of MIL@Cur within the needle tips (Fig. 4**C**). The microneedles were fabricated with consistent geometry, possessing a height of ∼ 500 μm, a base width of ∼ 250 μm, and a tip-to-tip spacing of ∼ 700 μm (Fig. 4**D**). Mechanical characterization through compression testing fully verified the structural robustness of the FCMN patch, demonstrating that needles prepared using a 10 % concentration hydrogel remained intact without fracture when subjected to pressures exceeding 0.4 N per needle (Fig. 4**E**). The drug release profile was evaluated in physiologically relevant media. When placed in different solutions, the FCMN achieved rapid and efficient release, with over 80 % of the loaded MIL@Cur released within 5 minutes (Fig. 4**F**). Upon application to mouse skin ex vivo, the needle tips dissolved efficiently, leaving behind a porous patch backing (Fig. 4**G**). Visualization of the treated skin via H&E staining confirmed the creation of microconduits with a penetration depth of 283.3 ± 7.6 μm (Fig. 4**H**) and a high penetration efficiency of 86.7 ± 4.2 % (Fig. 4**I**). To evaluate the local biocompatibility of the FCMN patch under conditions mimicking repeated application, a pilot study was conducted on healthy mice. FCMN patches were applied to the shaved dorsal skin daily for 10 minutes over three consecutive days. Daily macroscopic observation and histological analysis revealed no signs of irritation, such as redness, swelling, or scabbing (**Supplementary Fig. 5**).

In Vivo Therapeutic Efficacy in a Wound Infection Model

The therapeutic performance of the various formulations was rigorously assessed in a murine model of MRSA-infected full-thickness skin wounds. Macroscopic obser-

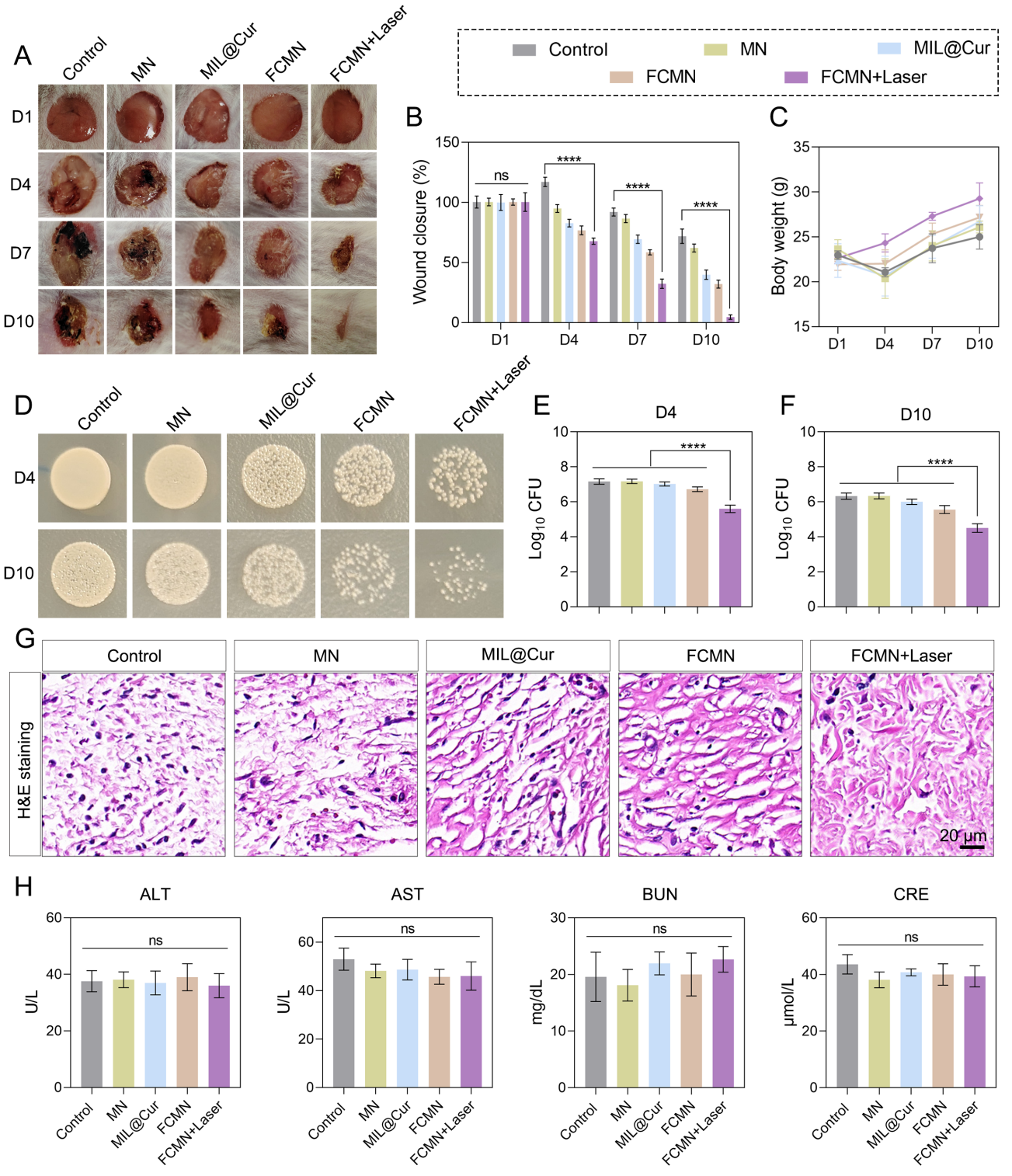

Fig. 5. ***In vivo*** **therapeutic efficacy in a murine wound infection model.** (**A**) Representative photographs and (**B**) corresponding quantitative healing rates of MRSA-infected wounds in different groups over 10 days. n = 3. (**C**) Body weight changes of mice throughout the treatment period. n = 3. (**D**) Photographs and quantitative bacterial load on (**E**) day 4 and (**F**) day 10 from wound homogenates. n = 3. (**G**) H&E staining of wound tissues on day 10. Scale bar: 20 μm. (**H**) Serum biochemical indicators of liver and kidney function on day 10. n = 3. MIL@Cur, curcumin-loaded iron-based metal-organic framework; MN, microneedle; FCMN, MIL@Cur microneedle; H&E, hematoxylin and eosin; ALT, alanine aminotransferase; AST, aspartate aminotransferase; BUN, blood urea nitrogen; CRE, creatinine; ns means no significant, ****$p < 0.0001$. The images were plotted using GraphPad Prism 9.0 and Adobe Photoshop 2023 software.

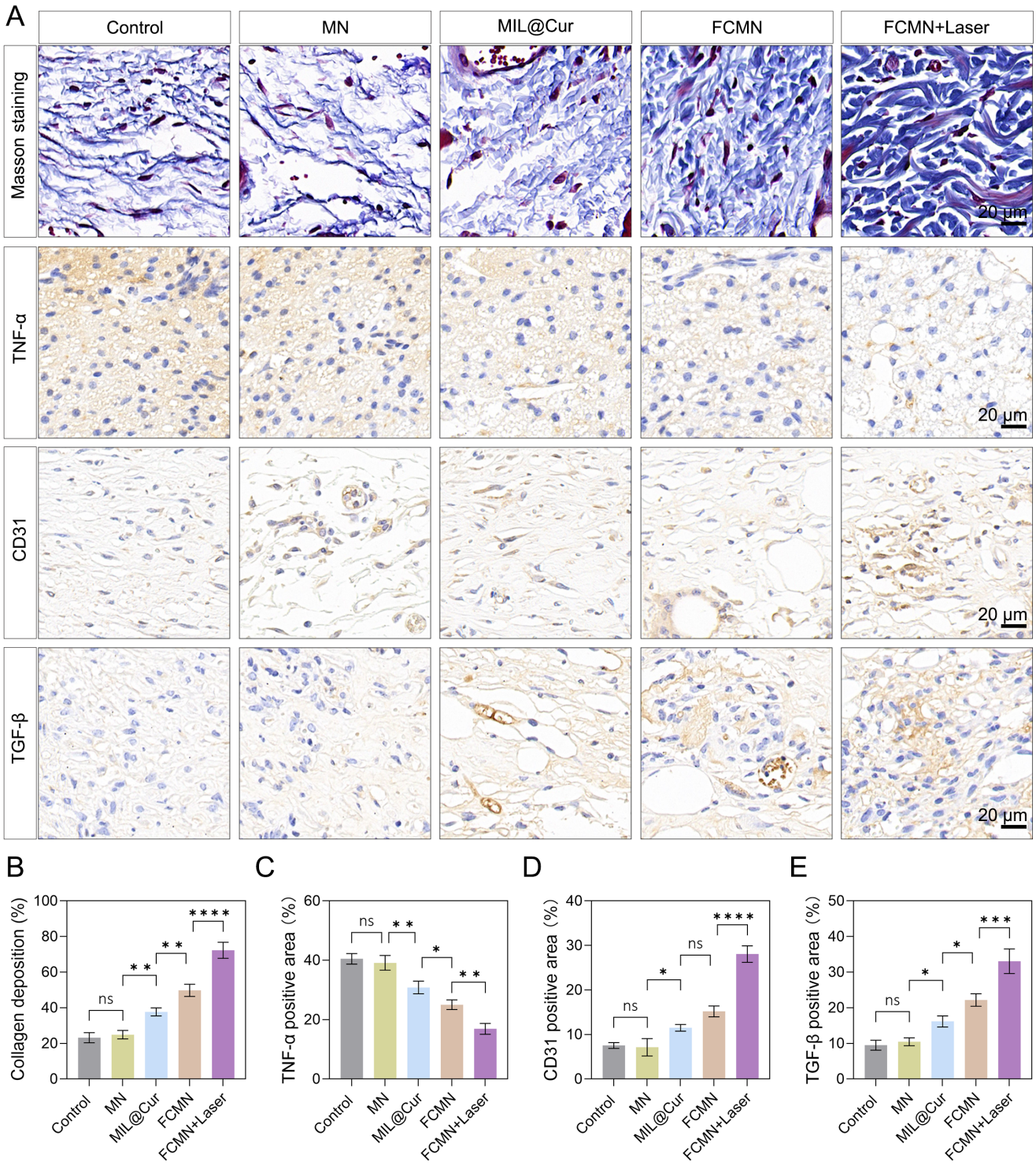

Fig. 6. Histological analysis of wound regeneration on day 10. (**A**) Representative images of Masson's trichrome staining and IHC staining for TNF-α, CD31, and TGF-β in wound tissues from different groups. Scale bars: 20 μm. Quantitative analysis of (**B**) collagen deposition area, (**C**) TNF-α positive area, (**D**) CD31 positive area, and (**E**) TGF-β positive area. n = 3. MIL@Cur, curcumin-loaded iron-based metal-organic framework; MN, microneedle; FCMN, MIL@Cur microneedle; IHC, immunohistochemical; TNF-α, tumor necrosis factor-α; CD31, platelet endothelial cell adhesion molecule-1; TGF-β, transforming growth factor-β. ns means no significant, *$p < 0.05$, **$p < 0.01$, ***$p < 0.001$, ****$p < 0.0001$. The images were plotted using GraphPad Prism 9.0 and Adobe Photoshop 2023 software.

vation over 10 days revealed distinct healing trajectories among the groups (Fig. 5**A, B**). The Control, MN, and MIL@Cur groups showed slow wound contraction, with persistent signs of infection such as erythema and pus. The FCMN group (without laser) demonstrated improved healing compared to the topical MIL@Cur group. However, the FCMN + Laser group exhibited the most rapid and complete wound closure, with the best visual appearance and minimal scarring, by the end of the study. Mice in this group also showed the most rapid body weight recovery (Fig. 5**C**). Bacterial counts from wound homogenates provided quantitative evidence for the treatment efficacy (Fig. 5**D–F**). On day 4, the FCMN + Laser treatment had already reduced the bacterial burden by about 1 log compared to the control. By day 10, this group achieved a substantial reduction of 2 logs, significantly outperforming all other groups, including the FCMN group without laser irradiation. Histological analysis of day-10 wound tissues via H&E staining correlated with these findings, revealing the least inflammatory cell infiltration and the most organized tissue structure in the FCMN + Laser group (Fig. 5**G**). Critically, blood biochemical analysis indicated no significant differences in liver (ALT, AST) and kidney (BUN, CRE) function markers among all groups (Fig. 5**H**). In addition, **Supplementary Fig. 6** showed no observable pathological abnormalities, necrosis, or inflammatory lesions in any of the examined organs from the FCMN + Laser group compared to the Control group.

Histological Analysis of Healed Wounds

A detailed histological analysis was conducted on day 10 to evaluate the quality of wound healing and the underlying tissue regeneration processes. Masson's trichrome staining revealed significant differences in collagen deposition among the groups (Fig. 6**A, B**). Tissues from the FCMN + Laser group showed the most abundant, dense, and well-organized collagen fibers. In contrast, the Control and MN groups displayed sparse and disorganized collagen deposition. The MIL@Cur and FCMN groups showed intermediate levels of collagen. IHC staining provided further mechanistic insights (Fig. 6**A**, **C–E**). The expression of the pro-inflammatory cytokine TNF-α was the lowest in the FCMN + Laser group. Conversely, the expression of the angiogenesis marker CD31 was the highest in this group. Similarly, the expression of the pro-regenerative growth factor TGF-β was significantly upregulated in the FCMN + Laser group.

Discussion

The relentless challenge of biofilm-associated infections in post-surgical care necessitates innovative therapeutic strategies that transcend conventional antibiotic paradigms. In this study, we have engineered an integrated microneedle-mediated platform that successfully addresses the dual barriers of skin penetration and biofilm resistance. This system synergistically co-delivers a photoresponsive iron-based MOF (MIL-101(Fe)) and the natural QS inhibitor curcumin, culminating in a potent multi-modal therapy for biofilm-infected wounds. The FCMN patch, upon NIR laser activation, demonstrates unparalleled efficacy in eradicating both planktonic and biofilm-embedded bacteria while actively promoting a pro-regenerative wound microenvironment.

The cornerstone of this platform's success is the rational design and meticulous characterization of the MIL@Cur nanohybrid. Our data confirm that the solvothermally synthesized MIL-101(Fe) possesses a highly uniform hexagonal star-like morphology, which remains intact after curcumin loading [31]. This structural preservation is paramount, as it maintains the high surface area and porosity essential for efficient photothermal conversion. The successful and homogeneous incorporation of curcumin within the MOF pores, corroborated by elemental mapping, ensures optimal loading and protects the labile QS inhibitor from premature degradation. Furthermore, the more negative zeta potential of MIL@Cur compared to its pristine counterpart signifies enhanced colloidal stability in aqueous media, a critical factor for reliable performance in physiological environments [32]. The nanohybrid's intelligent, stimuli-responsive behavior is evidenced by its accelerated release of both Fe ions and curcumin under acidic conditions (pH 5.0). This pH-triggered release profile strategically targets the acidic microenvironment characteristic of bacterial infection sites and biofilms, enabling a precise, on-demand therapeutic action [33,34]. When coupled with its exceptional and highly stable photothermal performance under 808 nm NIR laser irradiation—evidenced by a rapid temperature increase to over 50 °C and consistent performance across multiple irradiation cycles—the MIL@Cur nanohybrid establishes itself as an ideal core agent for a triggered, multi-modal antimicrobial strategy. This multifunctionality enables a concerted physical-chemical-biological attack that is fundamentally distinct from simply combining two separate materials, offering a more holistic strategy against complex biofilm infections.

The exceptional antibacterial and anti-biofilm outcomes observed both *in vitro* and *in vivo* can be deconstructed into a compelling triple-synergistic mechanism. First, the instantaneous photothermal effect upon NIR irradiation inflicts direct and irreparable physical damage to bacterial membranes [35]. This is quantitatively demonstrated by the marked increase in protein leakage and ONPG hydrolysis in the MIL@Cur + Laser group. This membrane disruption serves a dual purpose: it directly lyses bacterial cells and potently enhances the permeability of the biofilm matrix and bacterial envelopes, thereby facilitating the influx of subsequent therapeutic agents. Second, the localized heat acts as a smart trigger, explosively releasing a high concentration of Fe ions from the MOF framework.

These ions are rapidly internalized by bacteria, inducing a lethal state of iron overload. The subsequent Fenton reactions within the bacterial cells catalyze the conversion of endogenous H_2O_2 into highly cytotoxic hydroxyl radicals, leading to catastrophic oxidative stress. The pivotal role of this iron-mediated CDT is definitively proven by our rescue experiment, where pre-treatment with the iron chelator DFO significantly restored bacterial viability, as visually confirmed by the shift from red (dead) to green (live) fluorescence in live/dead staining. Third, operating concurrently with this physical and chemical assault, the released curcumin executes a sophisticated biological intervention. By potently suppressing the QS system—as molecularly evidenced by the significant downregulation of key genes (*agrA*, *AtlE*, *icaA*, *ica*D) governing adhesion and biofilm matrix synthesis—curcumin disrupts the very communication network that coordinates biofilm development and virulence [36,37]. This anti-virulence strategy, distinct from direct bactericidal action, effectively disarms the bacteria, sensitizing the biofilm structure to disintegration and crucially mitigating the potential for resistance development. The hierarchical efficacy observed across treatment groups, from the modest effects of free curcumin or MIL-101(Fe) alone to the profound synergy of the combined MIL@Cur + Laser treatment, underscores the necessity of integrating all three modalities.

The translation of this potent nano-agent from *in vitro* promise to *in vivo* reality was critically contingent upon the advanced design of the FCMN delivery platform. Dissolvable microneedles have emerged as a powerful tool for transdermal drug delivery, including for antimicrobials. However, most current systems are designed to deliver small molecules, peptides, or single-mode nanoparticles [38–40]. Our work advances this paradigm by engineering MNs for the co-delivery of a complex, multifunctional nanocomposite system (MIL@Cur). The patch features an array of microneedles with optimized geometry and demonstrable mechanical robustness, capable of withstanding pressures over 0.4 N per needle—far exceeding the force required for reliable skin penetration [41]. This capability was quantitatively verified by the high penetration efficiency ($\sim$ 87 %) and consistent depth ($\sim$ 283 μm) achieved in ex vivo skin, ensuring direct bypass of the stratum corneum barrier. The uniform distribution of MIL@Cur within the needle matrix, confirmed by elemental mapping, guarantees the coherent delivery of the full therapeutic payload. Crucially, the rapid dissolution of the hydrogel needles within minutes post-application enables the immediate and localized deposition of nano-agents directly into the wound bed and biofilm. This targeted delivery paradigm is instrumental in overcoming the dual defensive barriers of the skin and the biofilm's EPS, achieving high local drug concentrations precisely at the infection epicenter. The stark contrast in *in vivo* outcomes between the topical MIL@Cur application and the FCMN-mediated delivery, with the latter showing dramatically enhanced bacterial clearance and wound healing, irrefutably highlights the indispensability of this sophisticated delivery system to the platform's overall success.

Beyond achieving superior infection control, the FCMN + Laser therapy demonstrated a remarkable capacity to orchestrate a regenerative wound microenvironment. Histological analyses revealed that this combined treatment led to a significant reduction in the pro-inflammatory cytokine TNF-α, effectively resolving the chronic inflammation that impedes healing [42]. Concurrently, it promoted robust angiogenesis, as indicated by upregulated CD31 expression, ensuring adequate nutrient and oxygen supply [43,44]. The observed increase in TGF-β expression and the consequent deposition of abundant, well-organized collagen fibers, as seen in Masson's trichrome staining, are hallmarks of high-quality, functional tissue repair [45]. This shift from a stagnant, pro-inflammatory state to a dynamic, pro-regenerative phase underscores the therapy's ability to not only clear the pathogen but also to actively drive the wound healing process towards an optimal outcome [46].

Despite the promising results, several limitations of the current study should be acknowledged, which also point to directions for future research. First, the therapeutic efficacy was validated primarily in a subcutaneous wound model. The performance of this platform against deeper tissue infections or biofilm formation on medical implants remains to be investigated. Second, while this study thoroughly elucidated the intrinsic multi-mechanistic synergy of our platform, a direct comparative efficacy assessment against standard-of-care antimicrobials (e.g., topical vancomycin) was not conducted. Such comparisons in relevant infection models will be crucial for precisely defining its potential clinical advantage, especially in scenarios involving multidrug-resistant pathogens [47]. Third, regarding safety, our assessment confirmed the absence of acute systemic and local toxicity within the 10-day treatment window, coinciding with wound healing. However, a dedicated long-term study evaluating the biodistribution, metabolic fate, and safety of repeated application over extended periods would be a valuable next step in the translational pathway [48]. Addressing these aspects in future work will further solidify the platform's potential for clinical application against stubborn biofilm infections.

Conclusions

In conclusion, we have successfully developed a dissolvable microneedle patch that co-delivers a photoresponsive iron-based MOF and curcumin for highly effective treatment of biofilm infections. This platform synergistically combines photothermal therapy, iron-overload-mediated CDT, and QS inhibition, which collectively disrupt biofilms, eradicate embedded bacteria, and promote wound healing, as validated in both *in vitro* and *in vivo* mod-

els. This work provides a potent and clinically translatable strategy for combating multidrug-resistant bacterial infections without relying on traditional antibiotics.

List of Abbreviations

EPS, extracellular polymeric substance; MIL@Cur, curcumin-loaded iron-based metal-organic framework; MN, microneedle; FCMN, MIL@Cur microneedle; CDT, chemodynamic therapy; QS, quorum sensing; MOFs, metal-organic frameworks; TEM, transmission electron microscope; EDS, energy-dispersive X-ray spectroscopy; DLS, dynamic light scattering; CCK-8, cell counting kit-8; FBS, fetal bovine serum; PBS, phosphate-buffered saline; NIR, near-infrared; *S. aureus*, *staphylococcus aureus*; MRSA, methicillin-resistant *staphylococcus aureus*; *E. coli*, *Escherichia coli*; CFU, colony-forming units; ONPG, o-Nitrophenyl β-D-galactopyranoside; ROS, reactive oxygen species; DCFH-DA, 2′,7′-Dichlorodihydrofluorescein diacetate; DFO, deferoxamine; CLSM, confocal laser scanning microscopy; qRT-PCR, quantitative real-time polymerase chain reaction; PVA, poly(vinyl alcohol); PDMS, polydimethylsiloxane; SEM, scanning electron microscopy; H&E, hematoxylin and eosin; IHC, immunohistochemical; TNF-α, tumor necrosis factor-α; CD31, platelet endothelial cell adhesion molecule-1; TGF-β, transforming growth factor-β; ALT, alanine aminotransferase; AST, aspartate aminotransferase; BUN, blood urea nitrogen; CRE, creatinine; H_2O_2, hydrogen peroxide; DMF, N, N-Dimethylformamide.

Availability of Data and Materials

Data reported in this paper will be shared by the corresponding authors upon request. This paper does not report original code. Any additional information required to reanalyze the data reported in this paper is available from the corresponding authors upon request.

Author Contributions

FFC, ZYP and DDX contributed to the design of this work. LSZ, LYW and HYZ contributed to the interpretation of data. LSZ, KM, NNY and XLM analyzed the data. FFC and LYW drafted the work. ZYP and DDX revised critically for important intellectual content. All authors read and approved the final manuscript. All authors agreed to be accountable for all aspects of the work in ensuring that questions related to the accuracy or integrity of any part of the work were appropriately investigated and resolved.

Ethics Approval and Consent to Participate

Animal experiments were approved by the Ethics Committee of the Institutional Animal Care and Use Committee (IACUC) of Zhengzhou University (Approval No. 2023-KY-0433, Zhengzhou, China). All procedures were conducted in strict accordance with relevant ethical guidelines and regulatory standards. All animal experimental procedures were performed in accordance with ARRIVE guidelines 2.0.

Acknowledgments

The authors would like to thank Figdraw 2.0 platform for its support in creating the graphical abstract (https://www.figdraw.com).

Funding

This research was funded by the Youth Innovation Fund Project within the First Affiliated Hospital of Zhengzhou University (YNQN2017172) and the Medical Science and Technology Project of Henan Province (LHGJ20240264, LHGJ20240239).

Conflict of Interest

There are no conflicts of interest to declare.

Supplementary Material

Supplementary material associated with this article can be found, in the online version, at https://??.

References

[1] Jiang J, Lv X, Cheng H, Yang D, Xu W, Hu Y, *et al*. Type I photodynamic antimicrobial therapy: Principles, progress, and future perspectives. Acta Biomaterialia. 2024; 177: 1–19. https://doi.org/10.1016/j.actbio.2024.02.005.

[2] Li X, Li Q, He A, Dang M, Zhang Y, Wang M, *et al*. Disrupting Biofilm Tolerance by Ionic Microbubble-Mediated Copper Ion Surge for Infection Clearance. ACS Nano. 2025; 19: 28624–28643. https://doi.org/10.1021/acsnano.5c08035.

[3] Ouyang J, Bu Q, Tao N, Chen M, Liu H, Zhou J, *et al*. A facile and general method for synthesis of antibiotic-free protein-based hydrogel: Wound dressing for the eradication of drug-resistant bacteria and biofilms. Bioactive Materials. 2022; 18: 446–458. https://doi.org/10.1016/j.bioactmat.2022.03.033.

[4] Chung PY. Plant-derived Compounds as Potential Source of Novel Anti-Biofilm Agents Against Pseudomonas aeruginosa. Current Drug Targets. 2017; 18: 414–420. https://doi.org/10.2174/1389450117666161019102025.

[5] Mishra S, Gupta A, Upadhye V, Singh SC, Sinha RP, Häder DP. Therapeutic Strategies against Biofilm Infections. Life. 2023; 13: 172. https://doi.org/10.3390/life13010172.

[6] Costerton JW, Stewart PS, Greenberg EP. Bacterial biofilms: a common cause of persistent infections. Science. 1999; 284: 1318–1322. https://doi.org/10.1126/science.284.5418.1318.

[7] Roy R, Tiwari M, Donelli G, Tiwari V. Strategies for combating bacterial biofilms: A focus on anti-biofilm agents and their mechanisms of action. Virulence. 2018; 9: 522–554. https://doi.org/10.1080/21505594.2017.1313372.

[8] Brüssow H. The antibiotic resistance crisis and the development of new antibiotics. Microbial Biotechnology. 2024; 17: e14510. https://doi.org/10.1111/1751-7915.14510.

[9] Yao J, Zou P, Cui Y, Quan L, Gao C, Li Z, *et al*. Recent Advances in Strategies to Combat Bacterial Drug Resistance: Antimicrobial Materials and Drug Delivery Systems. Pharmaceutics. 2023; 15: 1188. https://doi.org/10.3390/pharmaceutics15041188.

[10] Johnson CT, García AJ. Scaffold-based anti-infection strategies in

bone repair. Annals of Biomedical Engineering. 2015; 43: 515–528. https://doi.org/10.1007/s10439-014-1205-3.

[11] Makabenta JMV, Nabawy A, Li CH, Schmidt-Malan S, Patel R, Rotello VM. Nanomaterial-based therapeutics for antibiotic-resistant bacterial infections. Nature Reviews. Microbiology. 2021; 19: 23–36. https://doi.org/10.1038/s41579-020-0420-1.

[12] He J, Hong M, Xie W, Chen Z, Chen D, Xie S. Progress and prospects of nanomaterials against resistant bacteria. Journal of Controlled Release: Official Journal of the Controlled Release Society. 2022; 351: 301–323. https://doi.org/10.1016/j.jconrel.2022.09.030.

[13] Miao B, Wang D, Yu L, Meng X, Liu S, Gao M, *et al*. Mechanism and nanotechnological-based therapeutics for tolerance and resistance of bacterial biofilms. Microbiological Research. 2025; 292: 127987. https://doi.org/10.1016/j.micres.2024.127987.

[14] Wang S, McGuirk CM, d'Aquino A, Mason JA, Mirkin CA. Metal-Organic Framework Nanoparticles. Advanced Materials. 2018; 30: e1800202. https://doi.org/10.1002/adma.201800202.

[15] Teixeira de Alencar Filho JM, Sampaio PA, Silva de Carvalho I, Rocha da Silva A, Pereira ECV, Araujo E Amariz I, *et al*. Metal organic frameworks (MOFs) with therapeutic and biomedical applications: a patent review. Expert Opinion on Therapeutic Patents. 2021; 31: 937–949. https://doi.org/10.1080/13543776.2021.1924149.

[16] Yang J, Yang YW. Metal-Organic Frameworks for Biomedical Applications. Small. 2020; 16: e1906846. https://doi.org/10.1002/smll.201906846.

[17] Zhu YD, Chen SP, Zhao H, Yang Y, Chen XQ, Sun J, *et al*. PPy@MIL-100 Nanoparticles as a pH- and Near-IR-Irradiation-Responsive Drug Carrier for Simultaneous Photothermal Therapy and Chemotherapy of Cancer Cells. ACS Applied Materials & Interfaces. 2016; 8: 34209–34217. https://doi.org/10.1021/acsami.6b11378.

[18] Liu X, Jin Y, Liu T, Yang S, Zhou M, Wang W, *et al*. Iron-Based Theranostic Nanoplatform for Improving Chemodynamic Therapy of Cancer. ACS Biomaterials Science & Engineering. 2020; 6: 4834–4845. https://doi.org/10.1021/acsbiomaterials.0c01009.

[19] Liu Z, Zhao X, Yu B, Zhao N, Zhang C, Xu FJ. Rough Carbon-Iron Oxide Nanohybrids for Near-Infrared-II Light-Responsive Synergistic Antibacterial Therapy. ACS Nano. 2021; 15: 7482–7490. https://doi.org/10.1021/acsnano.1c00894.

[20] Song H, Cheng Z, Qin R, Chen Z, Wang T, Wang Y, *et al*. Iron/Molybdenum Sulfide Nanozyme Cocatalytic Fenton Reaction for Photothermal/Chemodynamic Efficient Wound Healing. Langmuir: The ACS Journal of Surfaces and Colloids. 2024; 40: 14346–14354. https://doi.org/10.1021/acs.langmuir.4c00922.

[21] Zhu W, Mei J, Zhang X, Zhou J, Xu D, Su Z, *et al*. Photothermal Nanozyme-Based Microneedle Patch against Refractory Bacterial Biofilm Infection via Iron-Actuated Janus Ion Therapy. Advanced Materials. 2022; 34: e2207961. https://doi.org/10.1002/adma.202207961.

[22] Packiavathy IA, Sasikumar P, Pandian SK, Veera Ravi A. Prevention of quorum-sensing-mediated biofilm development and virulence factors production in Vibrio spp. by curcumin. Applied Microbiology and Biotechnology. 2013; 97: 10177–10187. https://doi.org/10.1007/s00253-013-4704-5.

[23] Zheng D, Huang C, Huang H, Zhao Y, Khan MRU, Zhao H, *et al*. Antibacterial Mechanism of Curcumin: A Review. Chemistry & Biodiversity. 2020; 17: e2000171. https://doi.org/10.1002/cbdv.202000171.

[24] Zhao C, Wu Z, Pan B, Zhang R, Golestani A, Feng Z, *et al*. Functional biomacromolecules-based microneedle patch for the treatment of diabetic wound. International Journal of Biological Macromolecules. 2024; 267: 131650. https://doi.org/10.1016/j.ijbiomac.2024.131650.

[25] Bu N, Li L, Hu X. Recent trends in natural polymer-based hydrogels for biomedical applications. Biofunctional Materials. 2024; 2: 0004. https://doi.org/10.55092/bm20230009.

[26] Ahmed Saeed Al-Japairai K, Mahmood S, Hamed Almurisi S, Reddy Venugopal J, Rebhi Hilles A, Azmana M, *et al*. Current trends in polymer microneedle for transdermal drug delivery. International Journal of Pharmaceutics. 2020; 587: 119673. https://doi.org/10.1016/j.ijpharm.2020.119673.

[27] Lyu S, Dong Z, Xu X, Bei HP, Yuen HY, James Cheung CW, *et al*. Going below and beyond the surface: Microneedle structure, materials, drugs, fabrication, and applications for wound healing and tissue regeneration. Bioactive Materials. 2023; 27: 303–326. https://doi.org/10.1016/j.bioactmat.2023.04.003.

[28] Wu ZF, Cheng W, Su JD. Progress in the application of microneedle-mediated cell implantation combined with artificial dermal scaffolds. European Cells and Materials. 2025; 53: 52–64. https://doi.org/10.22203/eCM.v053a05.

[29] Zhou J, Zhang L, Wei Y, Wu Q, Mao K, Wang X, *et al*. Photothermal Iron-Based Riboflavin Microneedles for the Treatment of Bacterial Keratitis via Ion Therapy and Immunomodulation. Advanced Healthcare Materials. 2024; 13: e2304448. https://doi.org/10.1002/adhm.202304448.

[30] Gholami S, Mohebi MM, Hajizadeh-Saffar E, Ghanian MH, Zarkesh I, Baharvand H. Fabrication of microporous inorganic microneedles by centrifugal casting method for transdermal extraction and delivery. International Journal of Pharmaceutics. 2019; 558: 299–310. https://doi.org/10.1016/j.ijpharm.2018.12.089.

[31] Gupta V, Tyagi S, Paul AK. Development of Biocompatible Iron-Carboxylate Metal Organic Frameworks for pH-Responsive Drug Delivery Application. Journal of Nanoscience and Nanotechnology. 2019; 19: 646–654. https://doi.org/10.1166/jnn.2019.15402.

[32] Midekessa G, Godakumara K, Ord J, Viil J, Lättekivi F, Dissanayake K, *et al*. Zeta Potential of Extracellular Vesicles: Toward Understanding the Attributes that Determine Colloidal Stability. ACS Omega. 2020; 5: 16701–16710. https://doi.org/10.1021/acsomega.0c01582.

[33] Ge Y, Wang K, Liu J, Tian Y, Li H, Wang H, *et al*. A ZIF-8-based multifunctional intelligent drug release system for chronic osteomyelitis. Colloids and Surfaces. B, Biointerfaces. 2022; 212: 112354. https://doi.org/10.1016/j.colsurfb.2022.112354.

[34] Shen X, Zhao D, Shi J, Li C, Bai Y, Qiu L, *et al*. Copper peroxide loaded gelatin/oxide dextran hydrogel with temperature and pH responsiveness for antibacterial and wound healing activity. International Journal of Biological Macromolecules. 2024; 274: 133258. https://doi.org/10.1016/j.ijbiomac.2024.133258.

[35] Zhang G, Li Z, Sun M, Lu Y, Song J, Duan W, *et al*. Nanostructure-Mediated Photothermal Effect for Reinforcing Physical Killing Activity of Nanorod Arrays. Advanced Science. 2025; 12: e2411997. https://doi.org/10.1002/advs.202411997.

[36] Hu H, Hua SY, Lin X, Lu F, Zhang W, Zhou L, *et al*. Hybrid Biomimetic Membrane Coated Particles-Mediated Bacterial Ferroptosis for Acute MRSA Pneumonia. ACS Nano. 2023; 17: 11692–11712. https://doi.org/10.1021/acsnano.3c02365.

[37] Mao Y, Liu P, Chen H, Wang Y, Li C, Wang Q. Baicalein Inhibits the *Staphylococcus aureus* Biofilm and the LuxS/AI-2 System *in vitro*. Infection and Drug Resistance. 2023; 16: 2861–2882. https://doi.org/10.2147/idr.S406243.

[38] Luo R, Xian D, Li F, Zhou G, Jiang L, Wu J, *et al*. Epsilon-poly-l-lysine microneedle patch loaded with amorphous doxycycline nanoparticles for synergistic treatment of skin infection. International Journal of Biological Macromolecules. 2024; 266: 131383. https://doi.org/10.1016/j.ijbiomac.2024.131383.

[39] Zhang J, Shi Y, Zhang Y, Fang Z, Zhou Y, Bian F, *et al*. Antibacterial and Proangiogenic Hydrogel Microneedle Patches for Wound Healing. Smart Medicine. 2025; 4: e70014. https://doi.org/10.1002/smmd.70014.

[40] Fang Y, Zhuo L, Yuan H, Zhao H, Zhang L. Construction of graphene quantum dot-based dissolving microneedle patches for the treatment of bacterial keratitis. International Journal of Pharmaceutics. 2023;

639: 122945. https://doi.org/10.1016/j.ijpharm.2023.122945.

[41] Tian S, Mei J, Zhang L, Wang S, Yuan Y, Li J, *et al*. Multifunctional Hydrogel Microneedle Patches Modulating Oxi-inflamm-aging for Diabetic Wound Healing. Small. 2024; 20: e2407340. https://doi.org/10.1002/smll.202407340.

[42] Patel S, Maheshwari A, Chandra A. Biomarkers for wound healing and their evaluation. Journal of Wound Care. 2016; 25: 46–55. https://doi.org/10.12968/jowc.2016.25.1.46.

[43] Yang Y, Wang P, Gong Y, Yu Z, Gan Y, Li P, *et al*. Curcumin-zinc framework encapsulated microneedle patch for promoting hair growth. Theranostics. 2023; 13: 3675–3688. https://doi.org/10.7150/thno.84118.

[44] Dai F, Zhang J, Chen F, Chen X, Lee CJ, Liang H, *et al*. A Multi-Responsive Hydrogel Combined With Mild Heat Stimulation Promotes Diabetic Wound Healing by Regulating Inflammatory and Enhancing Angiogenesis. Advanced Science. 2024; 11: e2408783. https://doi.org/10.1002/advs.202408783.

[45] Deng Z, Fan T, Xiao C, Tian H, Zheng Y, Li C, *et al*. TGF-β signaling in health, disease, and therapeutics. Signal Transduction and Targeted Therapy. 2024; 9: 61. https://doi.org/10.1038/s41392-024-01764-w.

[46] Raziyeva K, Kim Y, Zharkinbekov Z, Kassymbek K, Jimi S, Saparov A. Immunology of Acute and Chronic Wound Healing. Biomolecules. 2021; 11: 700. https://doi.org/10.3390/biom11050700.

[47] Kong J, Ma S, Chu R, Liu J, Yu H, Mao M, *et al*. Photothermal and Photocatalytic Glycol Chitosan and Polydopamine-Grafted Oxygen Vacancy Bismuth Oxyiodide (BiO_{1-x} I) Nanoparticles for the Diagnosis and Targeted Therapy of Diabetic Wounds. Advanced Materials. 2024; 36: e2307695. https://doi.org/10.1002/adma.202307695.

[48] Xie J, Zhou M, Cong Z, Xiao X, Liu L, Chen S, *et al*. A host defense peptide-mimicking prodrug activated by drug-resistant Gram-negative bacterial infections. Science Translational Medicine. 2025; 17: eadl4870. https://doi.org/10.1126/scitranslmed.adl4870.

Editor's note: The Scientific Editor responsible for this paper were Bo Lei and Martin Stoddart.

Received: 24th November 2025; **Accepted**: 26th January 2026; **Published**: 27th February 2026